The roles of surface-doped metal ions (V, Mn, Fe, Cu, Ce, and W) in the interfacial behavior of TiO$_2$ photocatalysts

Sue-min Chang [*], Wei-szu Liu [1]

Institute of Environmental Engineering, National Chiao Tung University, 1001, University Road, Hsinchu 30068, Taiwan

ABSTRACT

Six types of transition metal ions, including V, Mn, Fe, Cu, Ce, and W, are doped into the surface lattice of TiO$_2$ powders, and their roles in the charge trapping, recombination, interfacial transfer, and photocatalytic activity are systematically studied. The surface-doped TiO$_2$ powders exhibit photocatalytic activity in the order of Fe/TiO$_2$ > Cu/TiO$_2$ > V/TiO$_2$ > W/TiO$_2$ > Ce/TiO$_2$ > Mn/TiO$_2$. While the Fe, Cu and V ions improve the activity, the W, Ce, and Mn ions cause detrimental effects. The different influences are associated with their energy levels, coordination numbers and electronegativity. The surface-doped ions trap charge carriers and interact with adsorbates to provide alternative pathways for interfacial charge transfer. The Fe and Cu ions inhibit defect-mediated annihilation, facilitating interfacial charge transfer in terms of d–d transitions and thermally induced de-trapping. The Mn ions, which introduce both occupied and unoccupied states in the mid-band-gap region, in contrast, trap holes and electrons to severely consume charge carriers via intra-atomic relaxation. The Ce and W ions, which have high coordination numbers and electronegativity, strongly bond the O$_2{}^-$ radicals, thus limiting charge utilization as well as photocatalytic performance.

© 2014 Elsevier B.V. All rights reserved.

1. Introduction

Photocatalysts, which absorb photons to promote chemical reactions, have been considered as important green materials for environmental and energy applications [1,2]. Titanium dioxide (TiO$_2$) is the most used photocatalyst because it has high chemical stability, low toxicity, and solar sensitivity. In addition, its high density of states in bands enables efficient photon-to-current conversion, and leads to TiO$_2$ catalysts becoming more active than other semiconductors [3]. Photocatalytic activity correlates to the number of charge carriers which successfully escape from recombination and transfer to the adsorbates across the interface. To maintain a high level of effective charge carriers, doping transition metal ions into the TiO$_2$ lattice to inhibit recombination has been extensively studied [4,5].

Conventional doping incorporates ions homogeneously into the bulk lattice. The doped ions introduce additional energy levels into the band structure which are able to trap electrons or holes to separate charge carriers from the bands, thus allowing more charge carriers to successfully diffuse to the surface [5]. Depending on the types and the chemical states, transition metal ions provide different contributions to the photocatalytic activity. Xu et al. [4] improved the photocatalytic activity of TiO$_2$ nanoparticles by doping seven types of rare-earth ions individually into the TiO$_2$ matrix, and the enhancement is in the order of Gd^{3+} > Nd^{3+} > La^{3+} > Pr^{3+} (Er^{3+}) > Ce^{3+} > Sm^{3+}. Choi et al. [5] reported that doping TiO$_2$ colloids with Fe^{3+}, Mo^{5+}, Ru^{3+}, Os^{3+}, Re^{5+}, V^{4+}, and Rh^{3+} ions improves photoactivity, whereas Co^{3+} and Al^{3+} ions reduce the activity. The dopants with closed-shell configurations are considered to have little effect on the activity. In contrast, good dopants introduce their energy levels in the conduction/valence bands. Such dopants not only trap charge carriers in order to suppress band-to-band recombination, but also release the trapped carriers via thermal transition so as to maintain a high level of effective charge carriers. Similar de-trapping of shallowly trapped charge carriers also takes place in the dopants with the energy levels close to the band edges [7].

Although the improved activity of bulk-doped TiO$_2$ particles has been demonstrated, many studies have indicated that detrimental effects are the general consequence of doping because the trapped charge carriers quickly recombine with the counter carriers, irrespective of shallow or deep trapping [6,8,9]. The controversial
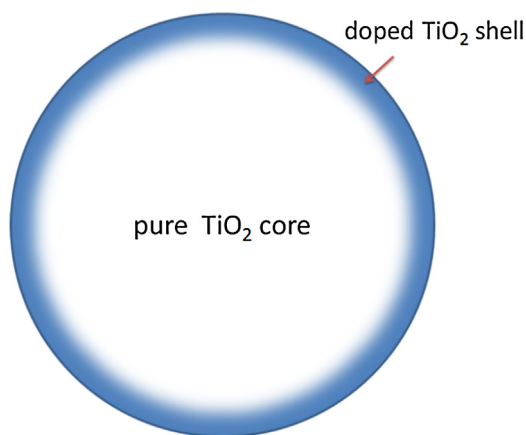
Fig. 1. The cross-sectional view of surface-doped TiO_2 particles.

effects of doping on the photocatalytic performance are attributed to the different doping amounts and the different sizes of doped photocatalysts. With the appropriate amounts of dopants, small sacrifices in charge carriers reduce the carrier density in the bands. The dopants thus inhibit band-to-band relaxation and allow a large fraction of the remaining carriers to successfully diffuse to the surface. The optimal loading for the highest photocatalytic performance is particle-size dependent. According to reported data, a model developed by Bloh et al. indicates that optimal doping amounts decrease with increasing particle sizes [10]. Heavy doping is unfavorable for large particles because it induces more defect-mediated recombination during the long journey of the carriers to the surface [11–13]. In contrast to the annihilation inside the bulk particles, the trapped charge carriers in the quantum-sized particles are able to reach the interface because their wave function spreads over the entire catalyst cluster [5].

To enable the trapped charge carriers to effectively participate in the surface reactions, V ions were doped into the surface lattice of micrometer-sized TiO_2 particles in a previous study [14]. In addition, the influences of surface doping and bulk doping on photocatalytic activity were clarified. It was found that the V ions within the surface lattice significantly enhance the activity as the concentration increases. In contrast, unless trace amounts of V ions are present, bulk doping reduces the activity. The surface-doped ions create an internal electric field to drive the charge carriers that are drifting from the bulk to the surface and suppress surface recombination via trapping, thus promoting charge utilization. Similar improvements where surface doping contributes to the activity are also demonstrated in the P^{5+}- and Zr^{4+}-doped TiO_2, the Zn^{2+}-doped SnO_2 and the Ba-doped $Cd_{0.8}Zn_{0.2}S$ powders [15–18]. Unlike the dopants within the bulk lattice, the surface-doped ions are involved in the adsorption and interfacial charge transfer in addition to trapping. The roles of different surface-doped ions in the interfacial behaviors and their contributions to the photocatalytic activity are still unclear.

In this study, we separately incorporate six different types of transition metal ions, including V, Mn, Fe, Cu, Ce, and W, into the TiO_2 surface lattice, and the photocatalytic activity of the surface-doped TiO_2 powders are systematically examined. Surface doping is carried out by coating as-prepared TiO_2 particles with a thin doped film followed by calcination. Fig. 1 shows the cross-sectional view of the surface-doped TiO_2 samples. To explore the different contributions to the activity by the surface-doped ions, we determine the charge trapping, recombination, and interfacial charge transfer at the surfaces. The roles of the dopants in the interfacial behaviors are elucidated with respect to their electronic structures, coordination numbers and elecotronegativity.

2. Experimental

2.1. Surface doping of TiO_2 photocatalysts with transition metal ions

Both pure and surface-doped TiO_2 samples were prepared using sol–gel processes, in which titanium isopropoxide (TTIP, Acros, 98%) compounds were used as the precursor for the TiO_2 powders. The TTIP liquid was diluted with isopropanol (IPA, J. Backer, 99.5%) to reach a molar ratio of TTIP/IPA = 1/30. The precursor solution was heated at 150 °C under ambient conditions for 3 h to induce hydrolysis and condensation. The solid was then calcined at 500 °C for 3 h to obtain pure TiO_2 powders. Surface-doped TiO_2 powders were prepared by coating the as-dried TiO_2 powders (2.0 g) with a thin doped TiO_2 film. The TiO_2 powders were dispersed in a coating solution that contains TTIP and transition metal ions (M) in IPA at a molar ratio of M/TTIP/IPA = 0.2/1.0/1200. Six types of transition metal ions, $VO(OC_3H_7)_3$ (VTIP, Aldrich, 99%), $Mn(NO_3)_2 \cdot 4H_2O$ (Merck), $Fe(NO_3)_3 \cdot 9H_2O$ (Riedel-de Haën), $CuCl_2 \cdot 2H_2O$ (SHOWA), WCl_6 (Aldrich), and $Ce(NO_3)_3 \cdot 6H_2O$ (SHOWA), were used as the dopants. To completely coat the TiO_2 particles with the coating solutions, the suspensions were treated using sonication for 10 min. Then, the powders were separated from the coating solution through centrifugation at 15,000 rpm for 3 min. After removing the supernatant, the remaining solution was further drained using suction. Simultaneously, the adsorbed precursors began to react with the water vapor in the ambient air to form a doped thin film on the TiO_2 surface. Prior to calcination at 500 °C for 3 h, the samples were dried at 100 °C to stabilize the structure of the films. Doping concentrations were adjusted by changing the M/TTIP ratios in the coating solution.

2.2. Characterizations

The morphology of the surface-doped TiO_2 powders was characterized using a transmission electron microscope (TEM, JOEL JEM-3000F) operated at an acceleration voltage of 300 kV. Elemental line-scanning and mapping analysis were measured using an energy-dispersive spectrometer (EDS) equipped in the TEM. The chemical states of the dopants and the chemical compositions were identified using an X-ray photoelectron spectrometer (XPS, PHI 1600) operated with an Al $K\alpha$ radiation (1486.6 eV). The photoelectrons were collected in the analyzer at a pass energy of 23.5 eV and at a collection interval of 0.1 eV. Chemical shifts resulting from the charging effects were calibrated by fixing the C 1s peak of the surface carbonaceous contaminants at 284.8 eV. The crystalline structures of the TiO_2 powders were examined using an X-ray powder diffractometer (XRPD, MAC Science, MXP18) with a Cu $K\alpha$ radiation ($\lambda = 1.5406$ Å), an accelerating voltage of 30 kV, and an emission current of 20 mA. The diffraction patterns were recorded at the 10–80° 2θ positions with a sampling width of 0.03° and a scanning speed of 10°/min. The electronic structures of the samples were analyzed using an UV–vis spectrometer (HITACHI 3010) in diffused reflectance mode with a scanning range from 900 to 200 nm. Aluminum oxide (Al_2O_3), which was considered to deliver total reflection, was used as the reference for all the measurements. The diffused reflectance was then converted into absorptions according to the Kubelka–Munk formula [19]. Nitrogen adsorption/desorption isotherms were measured using a gas sorption analyzer (Micromeritics, Tristar 3000) at 77 K. The Brunauer–Emmett–Teller (BET) model was used to estimate the surface areas of the samples based on the absorption data.

2.3. Charge trapping and interfacial transfer

Electron paramagnetic resonance (EPR) spectra were recorded using a Bruker EMX spectrometer operated at an X-band frequency. A 500 W Xe lamp (Ushio Inc.), with its major output wavelength set to 365 nm, served as the light source for the activation of the photocatalysts and was positioned at a fixed distance from a sample cavity. Prior to the analysis, the powders in the sample tubes were evacuated at 120 °C for 2 h to remove adsorbed water from the surface. The spectra of the trapped charges in the photocatalysts were recorded at 77 K under a vacuum both in the darkness and with UV illumination. To examine the interfacial charge transfer from the surface to the adsorbates, the same tubes were subsequently filled with O_2 gas, and the spectra of the samples in the O_2 atmosphere were acquired using the same processes. The instrumental conditions were set at a center field of 3050 G and a sweep width of 6000.0 G. The microwave frequency was 9.65 GHz with a power of 15.0 mW.

2.4. Photocatalytic activity

The photocatalytic activities of the pure and the surface-doped TiO_2 powders were examined based on the degradation of bisphenol A (BPA, 20 mg/L) in an aqueous solution under the irradiation of 305 nm UV light. The catalysts were suspended ultrasonically in the BPA solutions in fused-silica tubes. Prior to irradiation, the suspension was purged using O_2 gas in darkness accompanied with stirring for 30 min to equilibrate the adsorption and desorption of BPA and to saturate the solution with O_2. The degradation of the BPA molecules was monitored by sampling the suspension at different intervals of irradiation time and analyzing the concentration of the molecules in the remaining solution using a high performance liquid chromatograph (HPLC, Waters Alliance 2695) equipped with a C18 column (5 μm, 4.6 mm × 250 mm) and a photodiode array detector (PDA, Waters 2996). The mobile phase was a methanol–water mixture (80/20, V/V) at a flow rate of 1.0 mL/min.

3. Results and discussion

3.1. Bulk characteristics of the surface-doped TiO_2 photocatalysts

Fig. 2 shows TEM image, EDS elemental line-scanning and mapping results for the Fe-doped TiO_2 particles. The sizes and shapes of the sol–gel-derived TiO_2 powders were irregular, and most were at a nanometer scale. High concentrations of Fe elements were measured in the edges of the particles at a thickness of 10–20 nm. This result reveals the surface-doped feature of the sample. Other doped powders exhibited similar morphologies, but had thinner doped layers (<10 nm). The bulk properties, including the crystalline structures, the electronic structures and the surface areas, of the samples were examined using XRD, UV–vis spectroscopy, and N_2 adsorption–desorption measurement, respectively (see Supplementary materials, Table S1). Pure TiO_2 powders exhibited an anatase phase with a crystallite size of 16.5 nm. The band gap of the TiO_2 particles was 3.28 eV, which is close to that of bulk anatase TiO_2 crystals [20]. Surface doping with transition metal ions, including V, Mn, Fe, Cu, Ce, and W, had little effect on the bulk crystalline structures, and similar sized anatase TiO_2 crystals (14.8–16.8 nm) were also measured in the surface-doped powders. An insignificant shift in the (1 0 1) diffraction peak ($2\theta = 25.29$–25.32) indicates that the doped ions mainly remain within the surface lattice, and thermally-induced inward migration is unfavorable (see Supplementary materials, Fig. S1). These doped ions slightly inhibited particle coalescence and increased the specific surface area of the TiO_2 powders from 48 to 52–60 m^2/g. The doped TiO_2 powders had
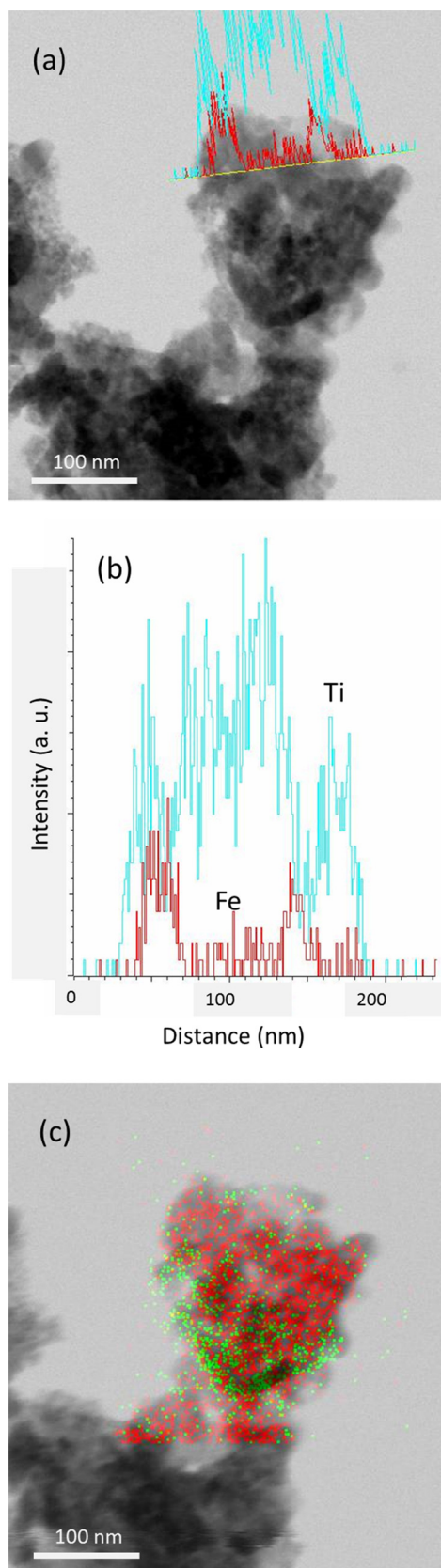

Fig. 2. (a) TEM image, (b) EDS line-scanning and (c) mapping results for the Fe-doped TiO_2 particles. Green and red dots in the mapping result stand for Fe and Ti elements, respectively. (For interpretation of the references to color in this figure legend, the reader is referred to the web version of this article.)

Table 1
The M/Ti ratios, chemical states, and the peak features of the photoelectron lines of doped transition-metal ions.

Dopant	XPS-surface					XPS-subsurface				EPR
	BE[a] (eV)	DS[b] (eV)	FWHM[c] (eV)	Chemical states	M/Ti ratios	BE[a] (eV)	DS[b] (eV)	FWHM[c] (eV)	Chemical states	Chemical states
V	516.7	7.6	1.5	V^{4+}	0.05	516.6	7.6	1.5	V^{4+}	V^{4+} (V^{3+})[d]
Mn	641.6	11.5	4.0	Mn^{3+}	0.11	641.5	11.5	4.5	Mn^{3+}	Mn^{4+} (Mn^{3+})
Fe	710.8	13.1	5.0	Fe^{3+}	0.48	709.6	13.6	4.0	Fe^{2+}	Fe^{3+} (Fe^{2+})
Cu	933.0	19.9	2.0	Cu^{+}	0.11	932.7	19.9	2.5	Cu^{+}	Cu^{2+} (Cu^{+})
Ce	886.1	18.5	4.5	Ce^{0} (55)[e]	0.09	885.7	18.5	4.5	Ce^{0} (66)	Ce^{0}, Ce^{4+}
	882.0	18.1	4.0	Ce^{4+} (45)		881.6	18.3	4.0	Ce^{4+} (34)	
W	36.3	2.2	1.8	W^{6+}	0.12	35.9	2.2	1.7	W^{6+}	W^{6+}

[a] BE—binding energy.
[b] DS: energy difference between the doublet splitting peaks.
[c] FWHM—full width at half maximum.
[d] The species in the parentheses are determined based on the increased intensity of oxidized species in the EPR spectra after exposure to O_2 molecules.
[e] Values in the parentheses are the atomic percentage of the species.

an intrinsic band gap of 3.21–3.31 eV. In addition, the surface-doped V, Mn, and Fe ions introduced extrinsic band gaps of 2.73, 2.54, and 2.15 eV, respectively, in the doped domain.

3.2. Surface compositions and chemical states of dopants

The surface compositions and the chemical states of the dopants were characterized using both XPS and EPR methods. The XPS spectra of the dopants in the top-most and sub-surface layers were acquired both before and after soft Ar sputtering. To ensure that the soft sputtering did not induce reduction of the doped ions in the samples, Fe_2O_3 powders were used as the standard and the photoelectron lines of the Fe ions were measured both before and after the sputtering. A minute chemical shift between the photoelectron peaks confirms that this action has little influence on changing the chemical states. Table 1 summarizes M/Ti ratios (M denotes the transition metal ions), the chemical states of the dopants, and detailed features of their corresponding photoelectron lines in the XPS spectra. The majority of the measured M/Ti ratios of the doped powders (0.05–0.12) were less than the nominal value (0.20), except for the Fe-doped TiO_2 sample, which had an Fe/Ti ratio of 0.48. The low M/Ti ratios are as the result of the reduced thicknesses of the doped shells (<10 nm) compared to the sampling depth of XPS. In fact, the surface Fe/Ti ratio was 0.22 prior to calcination. The increase in the ratio after calcination indicates that calcination forces the Fe ions to move toward the surface. The segregation of the Fe ions is due to their low solubility in the TiO_2 matrix and the Hüttig temperatures of iron oxides (defined empirically as 0.3 T_m, where T_m is the melting point. Fe_2O_3: 470 °C, FeO: 413 °C) that are lower than the calcination temperature (500 °C) [21,22]. Although Mn-, V-, and Cu-based oxides also have low Hüttig temperatures (Mn_2O_3: 266 °C, V_2O_5: 207 °C, CuO: 316 °C, Cu_2O: 289 °C), increased M/Ti ratios are not measurable using XPS because of the ultra-thin coating of the doped shells [23].

The states of the transition metal ions, V^{4+}, Mn^{3+}, Fe^{3+}, Cu^{+}, Ce^{0}/Ce^{4+}, and W^{6+}, were characterized in the top-most lattice. Except for the W^{6+} and Fe^{3+} ions, which maintain the same valence numbers as those of their precursors, the V^{4+}, Cu^{+}, and Ce^{0} species are the reduced forms, and the Mn^{3+} and Ce^{4+} ions are the oxidized forms of their precursors. After removal of several atomic layers using soft sputtering, we determined the chemical states of the dopants located within the sub-surface lattice. While the other doped ions exhibited the same chemical states as those in the outer lattice, reduced Fe^{2+} species and an increased fraction of Ce^{0} atoms were measured. The Fe^{3+} and V^{5+} ions could have been reduced by the isopropanol in the precursor solutions because the reduction potential of the Fe^{3+}/Fe^{2+} (0.711 V) and the V^{5+}/V^{4+} (E^0 = 1.00 V) couples is higher than that of isopropanol/acetone
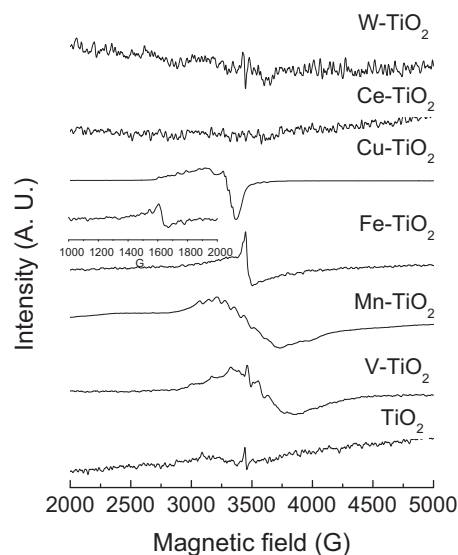

Fig. 3. EPR spectra for both the pure and the M-doped TiO_2 powders (M = V, Mn, Fe, Cu, Ce, and W ions within the surface lattice). All spectra are recorded in darkness in the vacuum.

(E^0 = 0.28 V) [14,24]. Moreover, thermally-induced dehydroxylation and deoxygenation also force the reduction of the doped ions [24,25]. The exposure of surface Fe ions to O_2 molecules at high temperatures dominates the Fe^{3+} state in the top-most layer. In contrast to reduction, Mn^{2+}-to-Mn^{3+} conversion occurs via the thermal decomposition of a MnO_2 moiety at about 500 °C [26]. The incompatible structure of the MnO moiety in the TiO_2 matrix could be the reason for the MnO-to-MnO_2 transformation at low temperatures. The disproportionation of the Ce^{3+} ions leads to the coexistence of the oxidized Ce^{4+} and reduced Ce^{0} species.

Fig. 3 shows the EPR spectra for the pure and the surface-doped TiO_2 powders recorded in a vacuum. EPR is sensitive to paramagnetic species and provides additional information about the chemical states of the dopants. The pure TiO_2 powders exhibited a weak signal at g = 2.003 in darkness, which denotes the trapped holes at the surface O^- species [15]. All the doped TiO_2 samples showed intensive peaks, other than the O^- signal, in their EPR spectra, indicating the paramagnetic features of the doped ions. V ions (S = 1/2, I = 7/2) in the doped TiO_2 powders contributed to an octet in the ERP spectrum as the result of nucleus hyperfine interactions. The simulated spin Hamiltonian parameters for the V ions are $g_\perp$ = 1.962, $A_\perp$ = 52 G, $g_{//}$ = 1.938, and $A_{//}$ = 165 G, indicating the V^{4+} ions [14]. The hyperfine interactions of ^{55}Mn elements (I = 5/2)
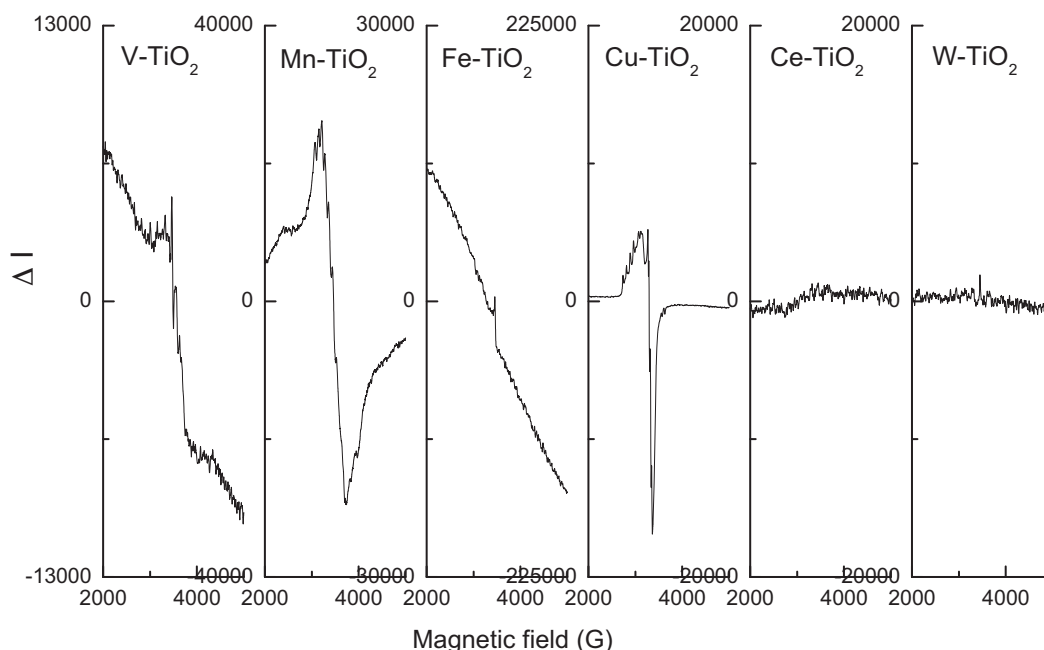
Fig. 4. EPR difference spectra for the M-doped TiO$_2$ powders. $\Delta I = I_{O_2} - I_{vac}$, where I_{O_2} and I_{vac} represent the intensity of the signals recorded in the O$_2$ atmosphere and in the vacuum, respectively.

showed two sets of sextet in the range of 2835–3976 G [27]. The simulated Hamiltonian parameters for the Mn ions are $g_x = 2.008$, $g_y = 1.994$, $g_z = 1.992$, and $A_{iso} = 86$ G, indicating the Mn^{4+} ions with a d^3 electronic configuration and $S = 3/2$. Mn^{3+} ions, which were examined as the major doped species in XPS, were silent in EPR. The Fe-doped TiO$_2$ sample showed two resonance peaks at $g = 4.3$ and 2.0, indicating the Fe^{3+} ions at the substitutional site in the anatase TiO$_2$ lattice [28]. Cu ions ($I = 3/2$) showed three sets of 4-fold hyperfine-structure lines, indicating Cu^{2+} ions with a d^9 electronic configuration. These peaks can be resolved using two groups of Hamiltonian parameters. The first is $g_\perp = 2.07$, $A_\perp = 30$ G, $g_{//} = 2.33$, $A_{//} = 70$ G, and the other is $g_\perp = 2.07$, $A_\perp = 30$ G, $g_{//} = 2.24$, $A_{//} = 70$ G, which indicate the Cu^{2+} ions at the substitutional sites and the Cu^{2+}

ions in the CuO cluster, respectively [29]. Ce and W ions were silent in the EPR spectra, revealing their diamagnetic properties. These results are in agreement with the chemical species (W^{6+}, Ce^{4+}, and Ce^0) determined from XPS. We further acquired the EPR spectra for the doped samples in the O$_2$ atmosphere to examine the interaction of the samples with O$_2$ molecules. Fig. 4 shows the EPR difference spectra obtained by subtracting the signals recorded in the vacuum from those recorded in the O$_2$ atmosphere. In the presence of O$_2$ molecules, the intensity of the V^{4+}, Mn^{4+}, Fe^{3+}, and Cu^{2+} species increased in the doped TiO$_2$ powders. These results reveal the existence of reduced species in the lattice, including V^{3+}, Mn^{3+}, Fe^{2+}, and Cu$^+$ ions. In addition, the doped ions are able to transfer electrons to the adsorbed O$_2$ molecules across the interface.
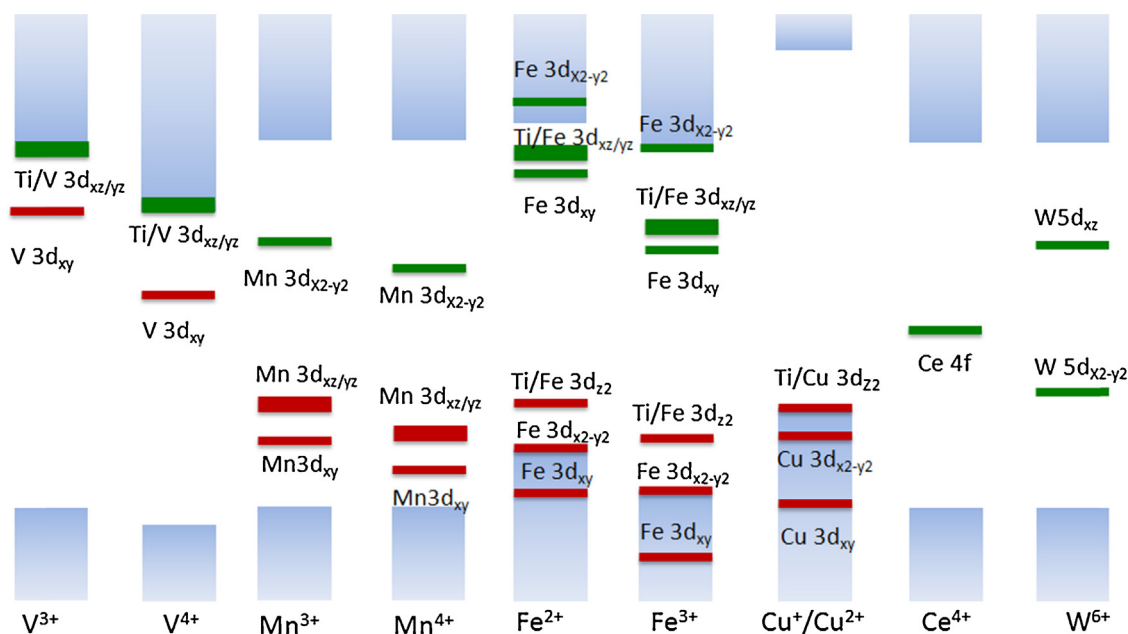

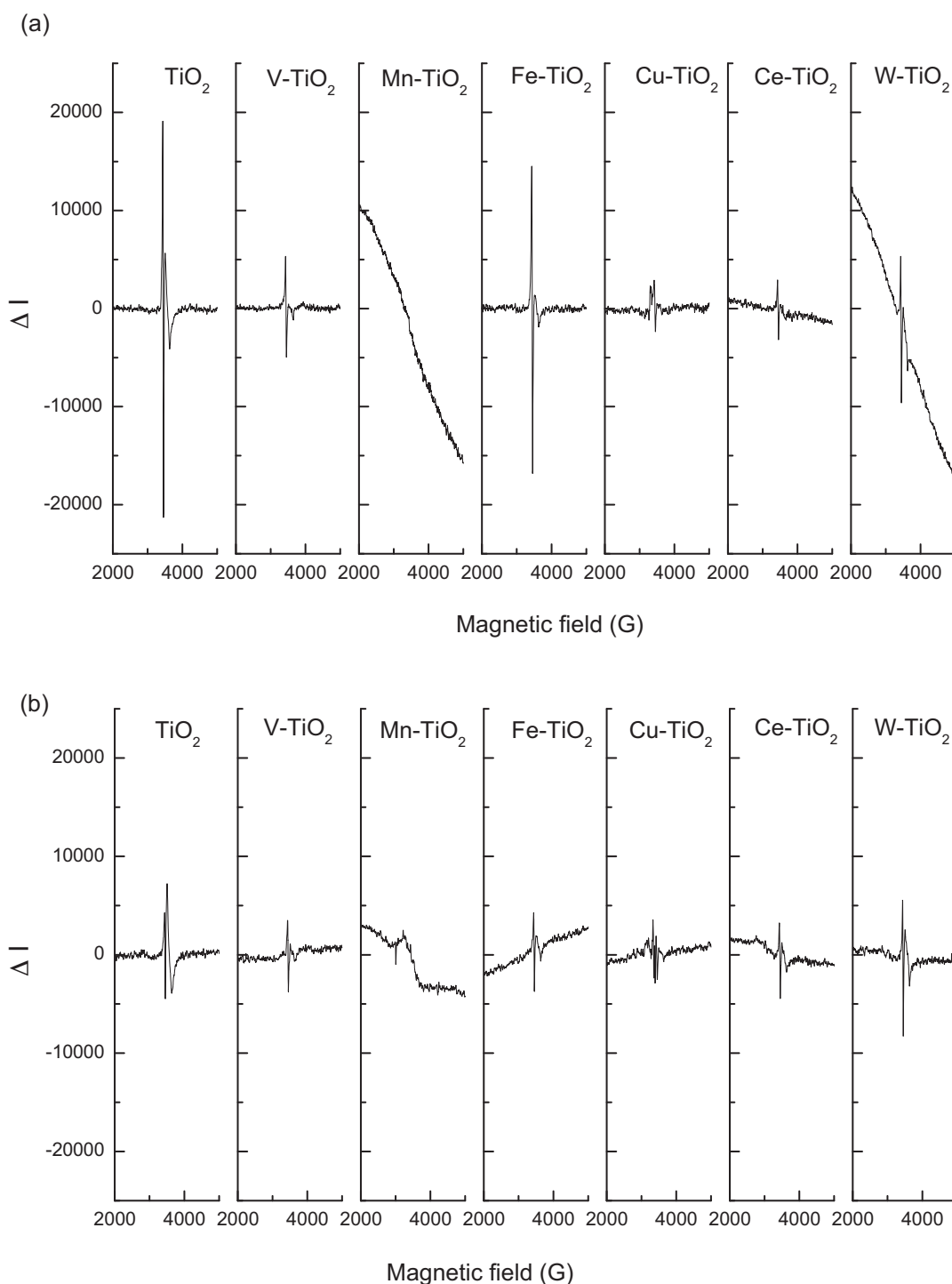
Fig. 5. Electronic structures of the surface-doped TiO$_2$ domains.

Fig. 6. EPR difference spectra for the pure and the surface-doped TiO_2 powders (a) in the vacuum and (b) in the O_2 atmosphere. $\Delta I = I_{irradiation} - I_{darkness}$, where $I_{darkness}$ and $I_{irradiation}$ represent the intensities acquired before and after irradiation, respectively.

Based on the species determined from XPS and EPR character-izations, we illustrate the electronic structures of the doped TiO_2 domains in Fig. 5. The conduction band and the valence band of TiO_2 matrix are primarily comprised of Ti(3d) and O(2p) orbitals, respectively [30]. When additional ions are introduced into the lat-tice, interaction between the outer-shell orbitals of these ions and the energy states in the bands creates impurity levels and changes the band structures. The influence of the dopants on the electronic structures is associated with their atomic numbers, ionic radii and oxidation states [30]. In general, the conduction band minimum (CBM) moves downward to a lower energy when a severe dis-tortion of the octahedral geometry is caused by small doped ions. The ions, which have high oxidation states, decrease the energy of both the valence band maximum (VBM) and the CBM because more oxygen ions are needed for charge compensation. The high occu-pancy of d-orbitals lowers the energy of the d states, thus moving the energy levels away from the conduction band and contributing to the VBM. In the V-doped TiO_2 domain, the de-localized d_{xz}/d_{yz} states of the V^{3+} and V^{4+} ions extend the CBM to a lower energy [30]. The occupied V^{3+} and V^{4+} $(3d_{xy})$ states are introduced at about

0.43 and 1.00 eV, respectively, below the CBM [31]. Doped Mn^{3+} ions have occupied $3d_{xy}$ and $3d_{xz}/3d_{yz}$ states positioned at 1.0 eV above the VBM and an unoccupied $3d_{x2-y2}$ states at 0.9 eV below the CBM [32,33]. Relative to the Mn^{3+} ions, the energy states of Mn^{4+} ions shift to lower energy values in the band gap [33]. The high splitting energy of Fe^{3+} ions introduces localized Fe $(3d_{x2-y2})$ states to the VBM to increase the band-edge energy. De-localized Ti^{4+}/Fe^{3+} $(3d_{z2})$ states, which are occupied with electrons, are positioned at 0.5–0.8 eV above the VBM, while the localized $Fe^{3+}(3d_{xy})$ and the delocalized Ti^{4+}/Fe^{3+} $(3d_{xz}/3d_{yz})$ states, which are unoccupied, are located at 0.7 eV below the CBM [30]. Fe^{2+} ions have a lower oxidation number and a larger ionic radii (0.78 Å) than Fe^{3+} ions (0.65 Å). Accordingly, the VBM of the Fe^{2+}-doped TiO_2 domains and the energy states of the Fe^{2+} ions move to higher energy values. Cu^+ ions have low potential d states because the d-orbitals are completely filled. The localized Cu^+ $(3d_{x2-y2})$ and the de-localized Ti^{4+}/Cu^+ $(3d_{z2})$ states dominate the VBM of the Cu-doped TiO_2 clusters and increase the band-edge to a higher energy [30,34]. Doped Cu^{2+} ions have energy states close to those of the Cu^+ ions in the band structure [34,35]. Ce^{4+} ions introduce unoccupied 4f states located at 1.5 eV below the CBM [36,37]. Two unoccupied states from the $W^{6+}(5d_{xz})$ and $(5d_{x2-y2})$ orbitals lie at 0.8 and 2.1 eV below the CBM, respectively [37,38]. These model simulations are in accordance with the electronic structures measured in this study. The extrinsic band gaps of the powders doped with V (2.73 eV), Mn (2.54 eV), and Fe (2.15 eV) ions correspond to the energy for the electron transition from the VBM to the de-localized V d_{xz}/d_{yz} states, the occupied Mn $3d_{xy}$ and $3d_{xz}/3d_{yz}$ states to the CBM, and the occupied Fe d states to the unoccupied d states, respectively [12].

3.3. Charge trapping, recombination and interfacial transfer

The doped ions within the surface lattice are involved in charge trapping, recombination and interfacial transfer. To ascertain these behaviors, we recorded the EPR spectra for the TiO_2 powders irradiated with UV light and semi-quantified the photo-generated species both in the absence and in the presence of O_2 molecules. Fig. 6 shows the EPR difference spectra for the pure and the doped TiO_2 powders both in the vacuum and in the O_2 atmosphere. The spectral differences are obtained by subtracting the spectra recorded in the darkness from those after irradiation, and the signals in the spectra indicate the photo-generated species. The quantities of the same species can be directly related to the corresponding intensities because all the samples have an equal mass and a similar surface area. The pure TiO_2 powders showed an intensive peak at $g = 2.003$ in the vacuum, indicating a substantial number of photo-generated holes trapped at the surface O^- sites. However, there were fewer the photo-generated holes in the O_2 atmosphere. Coronado et al. [39] reported that O_2 molecules are able to participate in the surface charge trapping by generating either ozonide ions ($Ti^{4+}-O_3^-$) or superoxide species ($Ti^{4+}-O_2^-$) when they react with the surface trapped holes or electrons, respectively. In this study, the disappearance of the photo-generated holes and the absence of $Ti^{4+}-O_3^-$ and $Ti^{4+}-O_2^-$ species indicate that the adsorbed O_2 molecules mediate charge recombination. In fact, surface O^- species disappeared when recorded in darkness after the pure TiO_2 powders were exposed to O_2 gas. This finding supports the understanding that the adsorbed O_2 molecules interact with the trapped holes.

Each of the dopants also eliminated the photo-generated holes to different extents when irradiated in the vacuum, and the holes were even unable to be detected in the Mn-doped samples. The doped ions, which introduce energy levels between the conduction and valence bands, are able to mediate charge annihilation
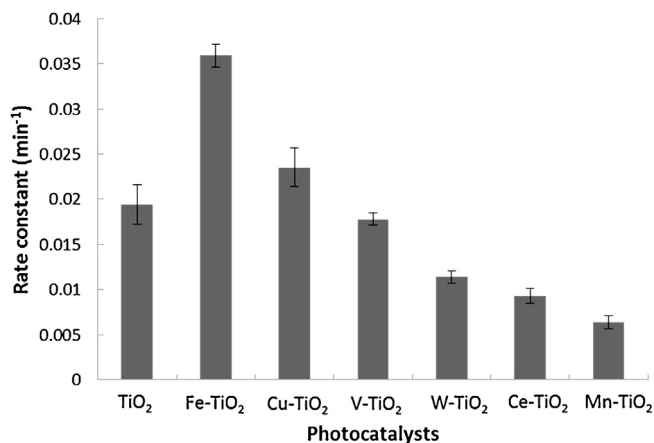
Fig. 7. The photocatalytic activity of the pure and the doped TiO_2 powders.

through trapping. Because there are no obvious signals of the dopants present in the difference spectra, mediated annihilation is rapid in all the doped samples. Based on the peak-to-peak heights, we semi-quantified the remaining trapped holes in the doped TiO_2 powders. It was found that Fe ions maintained the highest numbers of trapped holes, followed in order by W-, V-, Ce-, Cu-, and Mn-ions. The d–d transition of the Fe ions inhibits charge trapping and so reduces the mediated recombination. Compared to the V ions which introduce a single occupied state below the CBM, the two unoccupied states of the W ions mediate charge recombination more slowly because electrons require multiple processes to recombine with holes. The Ce-doped powders contained a substantial number of metallic Ce atoms. These metallic atoms mediate charge recombination by receiving electrons from the TiO_2 conduction band, and then returning the electrons to refill the holes in the valence band. Similar mediated recombination is also found at the interface between Pt nanoparticles and TiO_2 crystals [40]. Mn^{3+} and Mn^{4+} ions, which introduce both occupied and unoccupied levels in the mid-band-gap region, trap electrons and holes at almost the same time. Intra-atomic relaxation soon annihilates the trapped charge carriers. The occupied states of the Cu^+ and Cu^{2+} ions are positioned in the valence band. The remarkable reduction in the number of trapped holes and the slightly increased intensity of the Cu^{2+} peak indicate that the Cu ions are able to efficiently trap holes.

Through lattice trapping and interfacial transfer, both dopants and oxygen molecules are able to mediate recombination. To determine which process is more efficient, we compare the quantities of the trapped holes in the doped TiO_2 powders in the vacuum (Fig. 6a, doped powders) with those in the pure TiO_2 powders in the O_2 atmosphere (Fig. 6b, TiO_2). The higher intensities of the trapped holes in the Fe-, W-, and V-doped samples reveal that interfacial charge transfer from the conduction band to the adsorbed O_2 molecules is more efficient than the lattice trapping by the dopants, whereas, in contrast, the Ce, Cu, and Mn ions induced an opposite effect.

In the O_2 atmosphere, adsorbed O_2 molecules mediated recombination, and further eliminated the photo-generated holes in the doped TiO_2 powders. However, a reduction in the quantity of the holes of only 6% was found in the W-doped powders. Because charge transfer between the TiO_2 surface and the adsorbed O_2 molecules has been demonstrated to be faster than lattice trapping by the W ions, this small reduction suggests that the W ions inhibit the interaction of the O_2^- anions with the holes. Similar behavior was found on the Ce-doped powders, for which O_2 molecules even increased the number of photo-generated holes.
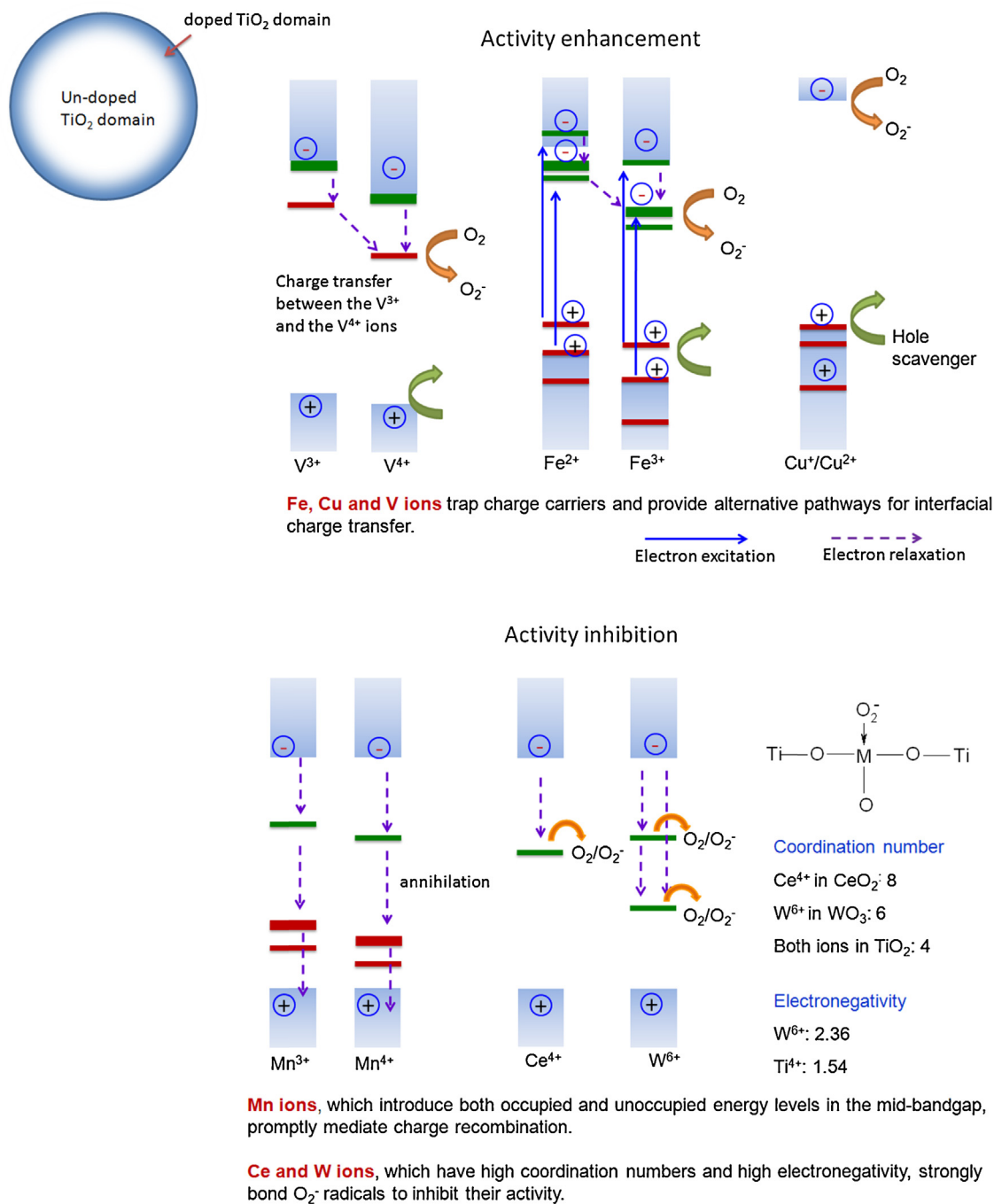
Fig. 8. The roles of the surface-doped ions in charge trapping, recombination, interfacial transfer, and interaction with surface species.

3.4. Photocatalytic activity

The photocatalytic activities of the pure and surface-doped TiO$_2$ powders were examined based on the degradation of BPA (20 mg/L) under UV irradiation. The degradation followed pseudo-first order kinetics, and the rate constants (k) were determined from the slope of the linear dependence between $\ln(C/C_0)$ and the reaction time, where C_0 and C are the BPA concentrations at the beginning and after a certain reaction time, respectively. Fig. 7 shows the photocatalytic activity of both the pure and doped powders. The photocatalysts exhibited activity in the order of Fe-doped TiO$_2$ ($k = 3.59 \times 10^{-2}$ min^{-1}) > Cu-doped TiO$_2$ ($k = 2.35 \times 10^{-2}$ min^{-1}) > TiO$_2$ ($k = 1.94 \times 10^{-2}$ min^{-1}) ~ V-doped TiO$_2$ ($k = 1.78 \times 10^{-2}$ min^{-1}) >

W-doped TiO$_2$ ($k = 1.14 \times 10^{-2}$ min^{-1}) > Ce-doped TiO$_2$ ($k = 9.33 \times 10^{-3}$ min^{-1}) > Mn-doped TiO$_2$ ($k = 6.40 \times 10^{-3}$ min^{-1}). We further optimized the Fe loading and found that the highest activity ($k = 3.88 \times 10^{-2}$ min^{-1}) occurred at a surface Fe/Ti ratio of 0.67 (see Supplementary materials, Fig. S2). This activity was two-times higher than that of the pure TiO$_2$ powders.

Photocatalysis is involved with charge generation, charge diffusion from the bulk to the surface, and interfacial charge transfer to the adsorbates. Charge recombination reduces the number of available charge carriers for the surface reactions, and is the key to low photocatalytic activity. Charge recombination occurs either through band-to-band relaxation or through defect-mediated annihilation. Incorporation of ions into the surface lattice creates an internal electric field to trigger the charge carriers to diffuse from

the bulk to the surface. In addition, surface-doped ions trap the charge carriers and inhibit band-to-band recombination. Unlike the dopants present in the photocatalysts, the dopants within the surface lattice are able to interact with adsorbates. Interfacial charge transfer via the surface-doped ions to the adsorbates competes with mediated annihilation to govern the photocatalytic activity, and the probability of these processes occurring is determined by the energy states, the coordination numbers and the electronegativity of the surface-doped ions.

Fig. 8 schematically illustrates the roles of the V, Mn, Fe, Cu, Ce, and W ions in the interfacial behaviors of the surface-doped TiO_2 photocatalysts. Surface-doped Fe and Cu ions improve the photocatalytic activity because they trap the charge carriers and interact with the adsorbates to provide alternative pathways for interfacial charge transfer. In addition, the d–d transitions of the Fe ions provide additional charge carriers to compensate for the charge recombination. The optimal surface Fe/Ti ratio for the highest photocatalytic activity is 0.67. Although this value is higher than the solubility of Fe ions (1–10 at.%) in the TiO_2 matrix, Fe_2O_3 clusters are too minute to be detected in the doped domain explored in this study [22,41]. Above this value, tunneling of the trapped carriers promotes annihilation and consequently reduce the photocatalytic activity [5]. Cu^+ ions, which introduce occupied and unoccupied states in the valence and conduction bands, respectively, efficiently trap the charge carriers. Moreover, the trapped charge carriers can leave the trapping sites and escape from recombination through thermally induced transition in the bands. The appearance of small Cu^{2+} signals in the EPR spectrum after irradiation supports this deduction (see Fig. 6). The electronic structure enables the surface-doped Cu ions to stabilize a high number of charge carriers at the surface, thus facilitating interfacial charge transfer. Surface-doped V ions have been demonstrated to improve the photocatalytic activity of the doped TiO_2 powders when the surface V/Ti ratio is higher than 0.14 [14]. However, the V ions examined in this study contribute little to the activity as a consequence of the low doping level (i.e. the V/Ti ratio is only 0.05). From the electronic structure point of view, $V^{3+/4+}$ ions have occupied states close the CBM. The high-energy states offer a thermodynamically favorable pathway and allow the electrons that have a high potential to undergo interfacial transfer through the V ions, and inhibit surface recombination.

In contrast to Fe, Cu, and V ions, surface-doped W, Ce, and Mn ions cause detrimental effects on the photocatalytic activity. The Mn and Ce elements reduce the activity because they serve as recombination centers. $Mn^{3+/4+}$ ions, which have both occupied and unoccupied states within the band gap, trap electrons and holes on the same sites and rapidly annihilate the trapped carriers through intra-atomic relaxation. Although the ions, which are able to trap both electrons and holes, are considered to effectively inhibit recombination via separating charge carriers on their different sites [42,43], we demonstrated, in this study, that such ions are more capable of promoting annihilation. Unlike Fe ions, d–d transition in the Mn ions is inactive in the irradiation spectrum. Charge recombination occurs too fast to allow interfacial transfer, thus consuming a substantial number of effective charge carriers. Metallic Ce elements are responsible for the severe recombination and the low activity of the Ce-doped TiO_2 powders. Schottky barrier at the hetero-junction has been extensively reported to effectively separate the charge carriers and enhance the photocatalytic activity [44]. However, the absence of electron receptors within the TiO_2 matrix forces the electrons that accumulate in the metallic Ce elements to refill the holes in the valence band of the TiO_2 matrix. In addition, the EPR result shows that the adsorbed O_2 molecules experience difficulty in mediating charge recombination on the Ce-doped TiO_2 powders. This phenomenon reveals that the surface Ce^{4+} ions strongly bind the chemisorbed $O_2{}^-$ radicals to inhibit the interaction of the radicals with the trapped holes.

Similar EPR features and low photocatalytic activity are also found in the W-doped-TiO_2-based system. These findings connect the low photocatalytic activity to the strong binding of $O_2{}^-$ radicals on the surface. We attribute this adverse effect to the high Lewis acidity of these doped ions. The W^{6+} and Ce^{4+} ions are 6- and 8-coordinated, respectively, in the WO_3 and CeO_2 moiety, whereas they are 4-coordinated in the TiO_2 matrix [45,46]. Unsaturated coordination allows these ions to bond with the $O_2{}^-$ radicals when they transfer the trapped electrons to the adsorbed O_2 molecules, or when the O_2 molecules receive electrons from the conduction band. Lewis acidity has been considered to improve photocatalytic activity because it promotes chemisorption of O_2 molecules to facilitate interfacial electron transfer [47–49]. However, the high electronegativity of the W^{6+} ions (Pauling's scale: 2.36) and the high oxygen deficiency of the Ce^{4+} ions lead the $O_2{}^-$ species to be tightly bound, consequently impeding subsequent interfacial charge transfer and reducing the activity.

4. Conclusions

The roles of V, Mn, Fe, Cu, Ce, and W ions in the interfacial behavior of surface-doped TiO_2 particles were systematically studied in terms of charge trapping, recombination, interfacial charge transfer and photocatalytic activity. The doped Fe, Cu and V ions improve the photocatalytic activity, whereas the Mn, Ce, and W ions cause adverse results. Surface-doped ions can either mediate charge recombination or transfer trapped carriers to adsorbates. The electronic structures, the coordination numbers and the electronegativity of the doped ions determine the probability of these two processes occurring and the photocatalytic activity of the surface-doped photocatalysts. Suitable dopants have d–d transitions in the irradiation spectrum, energy levels close to or within the conduction and valence bands, or multiple unoccupied states in the band gap. These electronic structures retard defect-mediated recombination and provide an alternative pathway that facilitates interfacial charge transfer via the doped ions. In contrast, unsuitable dopants promote recombination or confine the charge carriers at the surface, thereby inhibiting charge utilization. Such dopants introduce both occupied and unoccupied states in the mid-band-gap region, which trap electrons and holes to rapidly induce annihilation via intra-atomic relaxation. In addition, the ions with high coordination numbers or electronegativity strongly bond with $O_2{}^-$ radicals, thus limiting surface reactivity. The results in this study not only extend the knowledge related to the behaviors of surface-doped ions at the interface, but also provide important information to improve materials that exhibit high photon-to-current conversion efficiency.

Appendix A. Supplementary data

Supplementary data associated with this article can be found, in the online version, at http://dx.doi.org/10.1016/j.apcatb.2014.03.044.

References

[1] X.L. Hu, G.S. Li, J.C. Yu, Langmuir 26 (2010) 3031–3039.
[2] M. Anpo, Pure Appl. Chem. 72 (2000) 1265–1270.
[3] M. Quintana, T. Edvinsson, A. Hagfeldt, G. Boschloo, J. Phys. Chem. C 111 (2007) 1035–1041.

[4] A.W. Xu, Y. Gao, H.Q. Liu, J. Catal. 207 (2002) 151–157.
[5] W.Y. Choi, A. Termin, M.R. Hoffmann, J. Phys. Chem.—US 98 (1994) 13669–13679.
[6] K. Nagaveni, M.S. Hegde, G. Madras, J. Phys. Chem. B 108 (2004) 20204–20212.
[7] J.X. Li, J.H. Xu, W.L. Dai, H.X. Li, K.N. Fan, Appl. Catal., B: Environ. 85 (2009) 162–170.
[8] M. Schiavello, V. Augugliaro, L. Palmisano, K. Sclafani, A.M. Venezia, Langmuir 11 (1995) 3278.
[9] D. Dvoranova, V. Brezova, M. Mazur, M.A. Malati, Appl. Catal., B: Environ. 37 (2002) 91–105.
[10] J.Z. Bloh, R. Dillert, D.W. Bahnemann, J. Phys. Chem. C 116 (2012) 25558–25562.
[11] Z.B. Zhang, C.C. Wang, R. Zakaria, J.Y. Ying, J. Phys. Chem. B 102 (1998) 10871–10878.
[12] J.F. Zhu, F. Chen, J.L. Zhang, H.J. Chen, M. Anpo, J. Photochem. Photobiol., A: Chem. 180 (2006) 196–204.
[13] J.F. Zhu, Z.G. Deng, F. Chen, J.L. Zhang, H.J. Chen, M. Anpo, J.Z. Huang, L.Z. Zhang, Appl. Catal., B: Environ. 62 (2006) 329–335.
[14] S.M. Chang, W.S. Liu, Appl. Catal., B: Environ. 101 (2011) 333–342.
[15] S.M. Chang, P.H. Lo, C.T. Chang, Appl. Catal., B: Environ. 91 (2009) 619–627.
[16] S.M. Chang, C.Y. Hou, P.H. Lo, C.T. Chang, Appl. Catal., B: Environ. 90 (2009) 233–241.
[17] L.P. Li, J.J. Liu, Y.G. Su, G.S. Li, X.B. Chen, X.Q. Qiu, T.J. Yan, Nanotechnology 20 (2009).
[18] K. Zhang, Z.H. Zhou, L.J. Guo, Int. J. Hydrogen Energy 36 (2011) 9469–9478.
[19] S. Lacombe, H. Cardy, N. Soggiu, S. Blanc, J.L. Habib-Jiwan, J.P. Soumillion, Micro-porous Mesoporous Mater. 46 (2001) 311–325.
[20] H.J. Zhai, L.S. Wang, J. Am. Chem. Soc. 129 (2007) 3022–3026.
[21] J.A. Moulijn, A.E. van Diepen, F. Kapteijn, Appl. Catal., A: Gen. 212 (2001) 3–16.
[22] F. Gracia, J.P. Holgado, A. Caballero, A.R. Gonzalez-Elipe, J. Phys. Chem. B 108 (2004) 17466–17476.
[23] Q.L. Song, W. Liu, C.D. Bohn, R.N. Harper, E. Sivaniah, S.A. Scott, J.S. Dennis, Energy Environ. Sci. 6 (2013) 288–298.
[24] S.M. Chang, R.A. Doong, J. Phys. Chem. B 108 (2004) 18098–18103.
[25] S.M. Chang, R.A. Doong, Chem. Mater. 17 (2005) 4837–4844.
[26] J.H. Li, J.J. Chen, R. Ke, C.K. Luo, J.M. Hao, Catal. Commun. 8 (2007) 1896–1900.
[27] V. Singh, V. Natarajan, J.J. Zhu, Opt. Mater. 30 (2007) 468–472.

[28] C. Fabrega, T. Andreu, A. Cabot, J.R. Morante, J. Photochem. Photobiol., A: Chem. 211 (2010) 170–175.
[29] G.H. Li, N.M. Dimitrijevic, L. Chen, T. Rajh, K.A. Gray, J. Phys. Chem. C 112 (2008) 19040–19044.
[30] A.M. Shough, D.J. Doren, B. Ogunnaike, Chem. Mater. 21 (2009) 1232–1241.
[31] D.Y. Lee, W.J. Lee, J.S. Song, J.H. Koh, Y.S. Kim, Comput. Mater. Sci. 30 (2004) 383–388.
[32] A.L.J. Pereira, L. Gracia, A. Beltran, P.N. Lisboa, J.H.D. da Silva, J. Andres, J. Phys. Chem. C 116 (2012) 8753–8762.
[33] H.W. Peng, J.B. Li, S.S. Li, J.B. Xia, J. Phys. Condens. Matter 20 (2008).
[34] M.L. Guo, J.L. Du, Physica B: Condens. Matter 407 (2012) 1003–1007.
[35] N. Nakajima, H. Kato, T. Okazaki, Y. Sakisaka, Surf. Sci. 561 (2004) 93–100.
[36] W.G. Chen, P.F. Yuan, S. Zhang, Q. Sun, E.J. Liang, Y. Jia, Physica B: Condens. Matter 407 (2012) 1038–1043.
[37] H. Kamisaka, T. Suenaga, H. Nakamura, K. Yamashita, J. Phys. Chem. C 114 (2010) 12777–12783.
[38] R. Long, N.J. English, Appl. Phys. Lett. 98 (2011).
[39] J.M. Coronado, A.J. Maira, J.C. Conesa, K.L. Yeung, V. Augugliaro, J. Soria, Lang-muir 17 (2001) 5368–5374.
[40] W.N. Wang, W.J. An, B. Ramalingam, S. Mukherjee, D.M. Niedzwiedzki, S. Gangopadhyay, P. Biswas, J. Am. Chem. Soc. 134 (2012) 11276–11281.
[41] Q.P. Wu, Q. Zheng, R. van de Krol, J. Phys. Chem. C 116 (2012) 7219–7226.
[42] J.F. Zhu, W. Zheng, H.E. Bin, J.L. Zhang, M. Anpo, J. Mol. Catal. A: Chem. 216 (2004) 35–43.
[43] T.Z. Tong, J.L. Zhang, B.Z. Tian, F. Chen, D.N. He, J. Hazard. Mater. 155 (2008) 572–579.
[44] H. Chen, S. Chen, X. Quan, H.T. Yu, H.M. Zhao, Y.B. Zhang, J. Phys. Chem. C 112 (2008) 9285–9290.
[45] S. Yamazoe, Y. Masutani, T. Shishido, T. Tanaka, AIP. Conf. Proc. 882 (2007) 696–698.
[46] G. Dutta, U.V. Waghmare, T. Baidya, M.S. Hegde, K.R. Priolkar, P.R. Sarode, Chem. Mater. 18 (2006) 3249–3256.
[47] T.Z. Tong, J.L. Zhang, B.Z. Tian, F. Chen, D.N. He, M. Anpo, J. Colloid Interface Sci. 315 (2007) 382–388.
[48] Y. Cong, B.Z. Tian, J.L. Zhang, Appl. Catal., B: Environ. 101 (2011) 376–381.
[49] Y.F. Ma, J.L. Zhang, B.Z. Tian, F. Chen, L.Z. Wang, J. Hazard. Mater. 182 (2010) 386–393.